

In Situ Characterization of the Protein Corona of Nanoparticles In Vitro and In Vivo

Pierre-Luc Latreille, Jean-Michel Rabanel, Marine Le Goas, Sina Salimi, Jochen Arlt, Shunmoogum A. Patten, Charles Ramassamy, Patrice Hildgen, Vincent A. Martinez,* and Xavier Banquy*

A new theoretical framework that enables the use of differential dynamic microscopy (DDM) in fluorescence imaging mode to quantify in situ protein adsorption onto nanoparticles (NP) while simultaneously monitoring for NP aggregation is proposed. This methodology is used to elucidate the thermodynamic and kinetic properties of the protein corona (PC) in vitro and in vivo. The results show that protein adsorption triggers particle aggregation over a wide concentration range and that the formed aggregate structures can be quantified using the proposed methodology. Protein affinity for polystyrene (PS) NPs is observed to be dependent on particle concentration. For complex protein mixtures, this methodology identifies that the PC composition changes with the dilution of serum proteins, demonstrating a Vroman effect never quantitatively assessed in situ on NPs. Finally, DDM allows monitoring of the evolution of the PC in vivo. This results show that the PC composition evolves significantly over time in zebrafish larvae, confirming the inherently dynamic nature of the PC. The performance of the developed methodology allows to obtain quantitative insights into nano-bio interactions in a vast array of physiologically relevant conditions that will serve to further improve the design of nanomedicine.

1. Introduction

Nanomedicine offers new possibilities to increase the pharmaceutical efficacy of currently available drugs as well as to unleash novel therapeutic strategies, for example with the advent of gene therapy. During their travel in the blood stream, drug nanocarriers interact with blood proteins and often experience physical transformations of their size, shape, or aggregation, as well as chemical transformations at their surface. The interaction of free proteins with a nanoparticle's (NP) surface leads to the formation of the protein corona (PC), a protein shell whose structure and composition play a major role in the fate of nanoparticles in any living body.^[1–3] For instance, the presence of ApoE and clusterin proteins in the PC has been associated with slower clearance from the blood stream.^[4] Adsorption of other specific proteins has also been linked to enhanced brain translocation,^[5] hepatocyte targeting,^[6] reduced macrophage uptake,^[7] or an overall altered cellular uptake.^[8,9] An important consequence of the PC formation is the alteration or screening of targeting ligands of nanoparticulate drug delivery systems which ultimately impacts their therapeutic efficacy.^[10]

Attempts to characterize the PC's structure and formation mechanism have led to contrasting results. For example, transferrin was reported to form both multilayers and monolayers on a chemically identical system of sulfated polystyrene NPs.^[11,12] Bovine serum albumin (BSA) has also seen contrasting results, where monolayers^[13] and multilayers^[14] were both reported on metal NPs. Reversibility of protein adsorption on NPs has also been the subject of debates and controversies. Indeed, we recently showed that experimental evidence of the reversibility of protein adsorption was heavily dependent on the type of experiment used (dilution vs competition).^[15] These recent examples represent only a small fraction of the large body of studies from which no consensus has yet emerged on 1) whether protein adsorption on NPs surfaces should be considered as a reversible or irreversible phenomenon and 2) if the PC is structured as a mono- or multilayer.

Most techniques used to study the formation of the PC (e.g., mass spectrometry,^[16] fluorescence spectroscopy,^[17]

P.-L. Latreille, J.-M. Rabanel, M. Le Goas, S. Salimi, P. Hildgen, X. Banquy
Faculty of Pharmacy
Université de Montréal
PO Box 6128, Succursale Centre-ville
Montréal, Québec H3C 3J7, Canada
E-mail: xavier.banquy@umontreal.ca

J.-M. Rabanel, S. A. Patten, C. Ramassamy
INRS

Centre Armand Frappier Santé Biotechnologie
531 Boul des Prairies, Laval, Québec H7V 1B7, Canada

J. Arlt, V. A. Martinez
School of Physics and Astronomy
The University of Edinburgh

Peter Guthrie Tait Road, Edinburgh EH9 3FD, UK
E-mail: vincent.martinez@ed.ac.uk

 The ORCID identification number(s) for the author(s) of this article can be found under <https://doi.org/10.1002/adma.202203354>.

© 2022 The Authors. Advanced Materials published by Wiley-VCH GmbH. This is an open access article under the terms of the Creative Commons Attribution License, which permits use, distribution and reproduction in any medium, provided the original work is properly cited.

DOI: 10.1002/adma.202203354

UV-absorbance^[9] require to purify adsorbed proteins from free proteins using techniques (e.g., centrifugation, size exclusion)^[18] that can alter the PC structure and composition. Most techniques that enable in situ the quantification of adsorbed proteins are radius-based techniques (e.g., dynamic light scattering,^[19–21] fluorescence correlation spectroscopy,^[12,22–24] or even analytical ultracentrifugation^[25]). Such quantification methodology relies on the measurement of the variation of NPs size caused by protein adsorption, which is more sensitive for NPs and proteins of similar size.

Here we propose a new theoretical framework that enables the use of differential dynamic microscopy (DDM) in fluorescence imaging mode to quantify in situ protein adsorption onto NPs while simultaneously measuring NP size and aggregation. In this design, the proteins were fluorescently labeled, and NPs were not fluorescent. Upon protein adsorption onto unlabeled NPs, fluorescence signal is also emitted from the NPs surface. This emission produced measurable fluorescence fluctuations (due to the NPs Brownian diffusion) that are used to quantify the adsorption reaction from the measurement of separate contributions of free and adsorbed proteins. As shown below, due to its high selectivity and sensitivity for adsorbed proteins, DDM is able to provide information regarding the PC formation mechanism, its reversibility and its relation to NPs aggregation and stabilization both in vitro and in vivo, which has not been achieved in situ by any other technique so far. Using this approach, we highlight the affinity dependence of protein adsorption on NPs, a scaling that is observed with all proteins studied. Using more complex protein solutions, the developed methodology enables the identification of the Vroman effect at equilibrium in serum. Finally, we demonstrate that it is possible to generate with DDM quantitative in vivo measurements of protein desorption.

2. Theory of DDM in Fluorescence Imaging

DDM has been used to assess the dynamics of particles^[26] and bacteria^[27,28] in different imaging modalities such as confocal^[27] or standard microscopy using fluorescence,^[29] light-sheet,^[30] phase contrast,^[31,32] bright-field,^[26,33] and even dark-field.^[34] Here we focus on its application to a mixture of fluorescently labeled proteins and non-fluorescent NPs. In a DDM experiment, one record time-lapse microscopy images and calculates the power spectrum of the difference between pairs of images called the differential image correlation function (DICF) also known as the image structure function:

$$g(\bar{q}, \tau) = \langle (I(\bar{q}, t) - I(\bar{q}, t + \tau))^2 \rangle, \quad (1)$$

With $I(\bar{q})$ the Fourier transform of the image $I(\vec{r})$, \bar{q} the Fourier component or spatial frequency, τ the delay time, and brackets $\langle \dots \rangle_t$ denote the average over initial times t . In the present experimental study, the image (I) will be formed by the fluorescent signal emitted by both the protein free in solution (I_s) and the protein adsorbed onto NPs (I_{NP}) so that $I = I_s + I_{NP}$. Assuming I_s and I_{NP} are uncorrelated yields

$$g(q, \tau) = g_s(q, \tau) + g_{NP}(q, \tau) + B(q) \quad (2)$$

with $g_i(q, \tau) = A_i(q)(1 - f_i(q, \tau))$, $A_i(q)$ the amplitude of the DDM signal of the given component and $B(q)$ the experimental noise captured by the camera. Independent of the optical setup and technique, $B(q)$ is proportional to the total intensity in the image as it is related to the spontaneous fluctuations associated to the statistical distribution of photon counting from the camera.^[34] The dynamic parameter $f(q, \tau)$ is the intermediate scattering function (ISF) and $f(q, \tau) = \exp(-q^2 D \tau)$ for diffusive particles with diffusion coefficient $D = kT/(6\pi\eta R)$, where kT is the thermal energy, η the viscosity of the solvent, and R the hydrodynamic radius of the particles. In the present study, the radius of the proteins is orders of magnitude smaller than for NPs and thus we expect f_s to be well decoupled from f_{NP} . More specifically, we estimated $D_s = 140 \mu\text{m}^2 \text{s}^{-1}$ for lysozyme protein^[35] yielding a characteristic time $\tau_p = 1/(q^2 D_p) < 0.007\text{s}$ for $q > 1 \mu\text{m}^{-1}$. Therefore, by recording microscopy videos with an acquisition rate longer than τ_p , we expect f_s to have fully decorrelated and only the full decorrelation of f_{NP} will be measurable as f_{NP} will decorrelate with a characteristic time scale $\tau_{NP} > 0.01 \text{s}$ assuming $D_{NP} = 2.1 \mu\text{m}^2 \text{s}^{-1}$ (for $R = 110 \text{nm}$). With these conditions, Equation (2) can be approximated for $\tau \gg \tau_p$ to

$$g(q, \tau) \approx g_{NP}(q, \tau) + A_s(q) + B(q) = A_{NP}(q)(1 - f_{NP}(q, \tau)) + B^*(q) \quad (3)$$

While $B^*(q)$ that accounts for the camera noise $B(q)$ and the amplitude signal of free proteins $A_s(q)$ can be determined experimentally by identifying the short-time plateau of $g(q, \tau)$ at $\tau > \tau_p$, $A_{NP}(q)$ can be used to estimate the number of protein adsorbed onto NPs. The signal amplitude $A(q)$ depends on the signal generated by individual particles, their number density, and (in case of cluster formation or concentrated suspensions) on sample structure.^[31,36] For fluorescent NPs, this results in

$$A_{NP}(q) \propto C_{NP}^0 I_0^2 |A(q)|^2 S(q) \quad (4)$$

with I_0 the emitted fluorescence intensity per NP, $A(q)$ the single particle amplitude of detected light, C_{NP}^0 the number density of NPs, and $S(q)$ the suspension structure factor.

For fluorescently labeled proteins adsorbed onto non-fluorescent NPs, the detected intensity of the NP, I_0 , is directly related to the number of proteins adsorbed per particle, Γ , by $I_0 = \Gamma I_p$ with I_p being the (average) intensity of a single protein. Based on these considerations, Equation (4) can be expanded to obtain an expression for Γ

$$\Gamma = \left(\frac{A(q, C_p^0) C_{ES}^{NP}}{A(q)^{ES} C_{NP}} \right)^{1/2} \frac{I_0^{ES}}{I_p} \quad (5)$$

where $A(q, C_p^0)$ is the signal amplitude recorded at a total protein concentration C_p^0 (both adsorbed onto NPs and free in solution), and the superscript ES refers to the External Standard used to normalize the signal amplitude. The external standard is a suspension of fluorescently labeled PS NPs, identical in shape, size, and material to the probed unlabeled NPs. The adsorbed amount of protein can also be quantified using a relative method. In that case, the expression for Γ is

$$\Gamma = \Gamma_{\text{ref}} \left(\frac{A(q, C_p^0) C_{\text{ref}}^{\text{NP}}}{A(q, C_0^{\text{ref}}) C_{\text{NP}}} \right)^{1/2} \quad (6)$$

where the superscript “ref” refers to the reference state (RS). The factor Γ_{ref} is measured by an orthogonal method, for example fluorescence spectroscopy. Equation (5) assumes a linear relationship between I_0 and I_p . Therefore, in the limiting case of quenching between NPs and the fluorescent probe for example, the presented theoretical framework would require to be adapted or an alternative imaging modality should be used. Finally, as both methods rely on fluorescence intensity quantification, the measurement of adsorbed proteins is independent of the protein shape and size if the criteria defined previously are considered.

While the DDM signal amplitude allows us to measure amount of adsorbed proteins we can simultaneously monitor the size of the diffusers by measuring their diffusion coefficient D extracted by fitting $f_{\text{NP}}(q, \tau)$ over a range of q values. The relative increase in hydrodynamic radius due to an adsorbed layer of proteins is too small to be detected, but aggregation of NPs can lead to a large decrease in D .

3. Results and Discussions

3.1. Using the Amplitude Signal of DDM to Monitor Protein Adsorption

The experimental setup used to perform DDM experiments in the fluorescence imaging mode consists of a standard epifluorescence microscope equipped with a sCMOS camera. The processing workflow starting from the experimental design to the data acquisition and analysis is illustrated in **Figure 1A**. In brief, a fluorescently labeled protein solution of concentration C_p^0 is mixed with a NP suspension and the resulting mixture is introduced in a rectangular glass capillary of 400 μm in thickness and observed under the microscope. When illuminated at the excitation wavelength of the fluorescent protein, the emitted fluorescence light is detected by the camera sensor and time series of images are recorded. The motion of the free and adsorbed proteins creates localized fluctuations in the emitted intensity which are evaluated by DDM (see theory section).

Figure 1B represents the evolution of $g(q, \tau)$ and its main parameters for a suspension of PS NPs of hydrodynamic radius $R = 110$ nm in the presence of increasing concentrations of

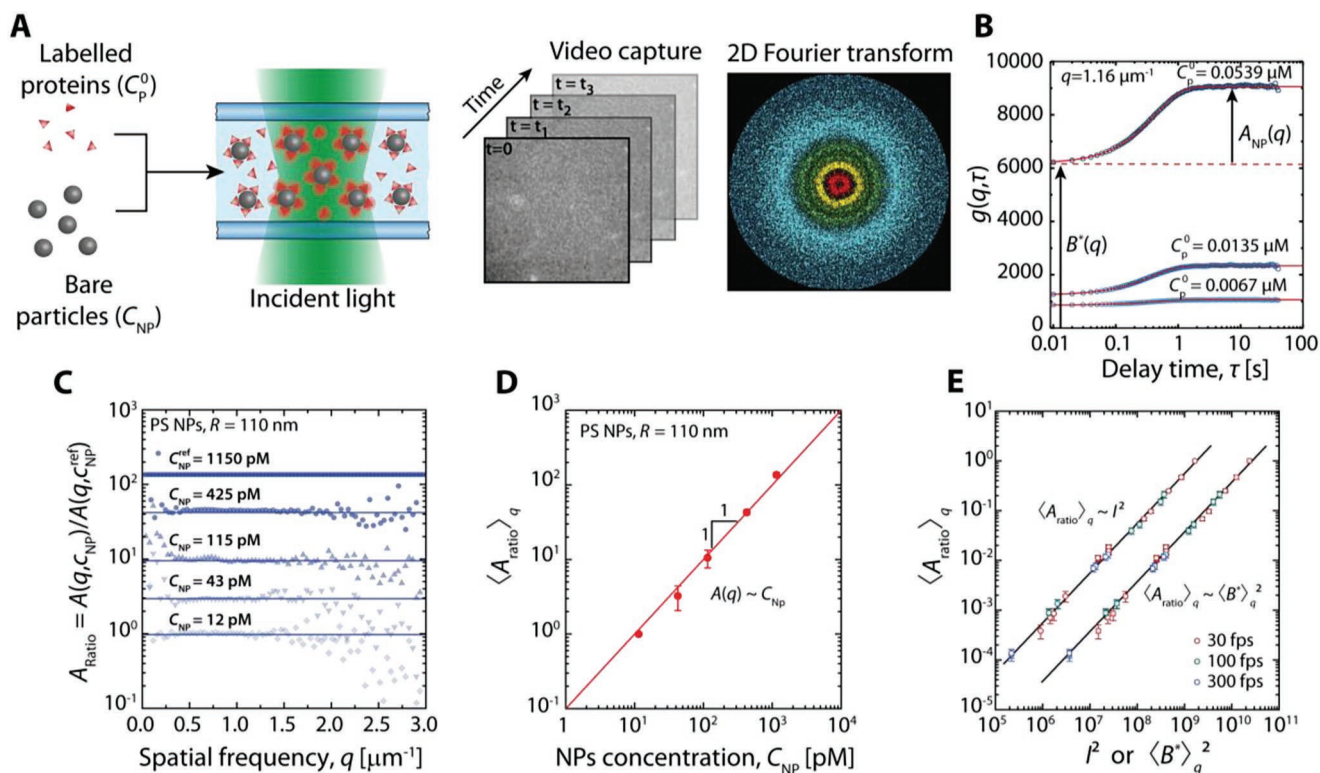


Figure 1. Demonstration of key parameters for the quantification of adsorbed proteins using DDM. A) The workflow to assess proteins adsorbed on NPs starts by mixing the NPs with labeled proteins and letting them adsorb. The suspension is then transferred into a glass capillary for fluorescence microscopy imaging. Time series of images are then analyzed following the process described in the text to extract the 2D Fourier transform and the DCF. B) Examples of DCF $g(q, \tau)$ obtained at different protein concentrations showing the values of parameters $A_{\text{NP}}(q)$ and $B^*(q)$ used for the quantification of the amount of protein adsorbed, where red solid curves are fits to Equation (3) $f(q, \tau) = \exp(-Dq^2\tau)$ for diffusive particles. C) Experimental evidence showing that the parameter A_{ratio} , which is directly proportional to the amount of adsorbed protein, is independent of the spatial frequency q and can therefore be averaged over q . D) Experimental validation of the linear relationship between A_{ratio} and the concentration of particles in the medium as predicted by Equation (4), represented by the red line. E) Validation of the power-law dependence (black lines) of A_{ratio} with the average total fluorescence intensity, independently of the frame rate used for the acquisition.

fluorescent proteins. One single decorrelation is observed with delay time τ while the short-time plateau $B^*(q)$ increases with C_p^0 in agreement with Equation (3). The increase of the DDM signal amplitude A_{NP} is the indication that protein adsorption of the NPs occurred. To verify this is the case and to measure protein adsorption on NPs from this signal, we demonstrate the applicability of Equations (4) and (5) to our experimental setup, notably its C_{NP} and I_0 dependence.

In Figure 1C,D, we experimentally validated the scaling $A_{ratio} \propto C_{NP}$ using suspensions of fluorescently labeled PS particles identical to the particles used for the protein adsorption experiments. As shown in the Figure 1D, a linear relationship between A_{ratio} and C_{NP} was observed over two orders of magnitude of C_{NP} , from 11.5 μM (diluted regime, volume fraction $\phi \approx 2.7 \times 10^{-4}$) up to 1150 μM (multiple scattering regime, $\phi \approx 2.7 \times 10^{-2}$). This attribute of DDM to test very large concentrations range of NPs (see Section S2 and Figure S2, Supporting Information) is not shared by other light-scattering techniques, especially DLS (and other related techniques) or fluorescence correlation spectroscopy (FCS).

The scaling of A_{ratio} with I_0^2 was also validated using the same fluorescently labeled NPs and modulating I_0 by changing the exposure time or the intensity from the excitation light source (see Figure 1E). We also verified that the impact of the experimental measurement conditions such as the size of the camera region of interest and the binning on $A_{NP}(q)$ could be accurately described and predicted (see Section S2 and Figure S2D,E, Supporting Information).

In typical experiments, C_{NP} is known or can be estimated, but I_0 and I_p must be quantified in order to obtain Γ from Equation (5). The intensity per protein is simply obtained by considering that the time- and pixel-averaged intensity per frame, I_{av} , is directly proportional to I_p (or I_0 for the external standard) and the concentration of fluorescent molecules. One can also take notice that $\langle B^* \rangle_q$ can be used as a substitute to I_{av} (see Figure 1E). Indeed, $\langle B^* \rangle_q^2$ is shown to be proportional to I_{av}^2 and simultaneously independent of the illumination mode and sample type (see Section S2 and Figure S2F, Supporting Information).

3.2. Monitoring of Protein–Particle Interactions In Situ

The methodology presented here was applied to the adsorption of fluorescently labeled LYZ protein (LYZ-RITC) on PS spheres of radius $R_0 = 110$ nm in buffered solution (pH = 7.4). The measured adsorption of lysozyme was obtained for total protein concentrations, C_p^0 , ranging from 0.05 to 100 μM , using either the ES (Equation (5)) or RS (Equation (6)) normalization (see Figure 2A-i). Both normalization methods were found equivalent since measurements for both methods overlapped and therefore were used interchangeably. Also shown in Figure 2A is the evolution of the particle size with the total protein concentration, which indicates the presence of strong NPs aggregation in a relatively narrow range of C_p^0 (1–4 μM) indicated as a gray area in Figure 2A-ii. Presence of aggregates is also confirmed by a strong q -dependence of the A_{ratio} as shown in Figure 2B-i. In this concentration window for which aggregation is not negligible, the aggregated particle intensity increases

to $I_{agg} = I_0 N$ and the concentration of particle or aggregate in the field of view decreases with $C_{NP-agg} = C_{NP} N^{-1}$ where N is the number of NPs per aggregate. Substitution in Equation (5) becomes $\Gamma_{agg} \approx \Gamma \sqrt{N}$, so that we can then extract Γ from the measured Γ_{agg}

$$\Gamma = \Gamma_{agg} / (N)^{1/2} \quad (7)$$

and N is given by $N = \left(\frac{R_N}{R_0} \right)^{d_f}$ where R_0 and R_N are the radius of gyration of a single NP and of an aggregate of N NPs respectively. The fractal dimension d_f can be quantified directly via the amplitude of the DDM signal (Equation (4)) and was also previously assessed by DDM from the kinetic measurement of the radius.^[33] Indeed, the structure factor $S(q)$ is related to the radius of gyration of the aggregate R_g and the fractal dimension d_f following the Fisher–Burford model^[33,37]

$$S(q) = \left[1 + \frac{2(qR_g)^2}{3d_f} \right]^{-d_f/2} \quad (8)$$

Substitution of Equation (8) into Equation (4) for aggregated NPs and considering $S(q) = 1$ for reference NPs from the ES method, as NPs concentration is low enough that interparticle

interactions are negligible, the measured $A_{ratio}(q) = \frac{A(q, C_p^0)}{A(q)^{ES}}$ will

become q -dependent from the structure factor of the aggregate. The q -dependence of A_{ratio} is evaluated by fitting it with Equation (8) as a function of q (see Figure 2B-i), from which both R_g and d_f are extracted. We confirmed that DDM can quantitatively assess d_f in situ by comparing with independent methods (see Figure S3, Supporting Information).

We show in Figure 2A-i, in the strong aggregation regime, $d_f = 1.61 \pm 0.19$, suggesting that aggregates are formed via a diffusion limited colloid aggregation (DLCA) mechanism as opposed to reaction-limited colloid aggregation mechanism (RLCA) for which $d_f \approx 2.1$ – 2.2 is expected.^[33,38] Figure 2B-ii also provides an example of time evolution of d_f in the strong aggregation regime. As can be seen, d_f reaches a constant $d_f \approx 1.5$ within 10 min for almost an hour, after which signs of sedimentation were observed.

The effect of aggregation of NPs induced by the adsorption of proteins has already been reported,^[12,21,39] but so far its impact on protein adsorption has not been evaluated. The data shown in Figure 2A demonstrate that protein adsorption is not affected by particle aggregation. Comparison of the kinetics of aggregation with the kinetics of protein adsorption clearly shows that LYZ adsorbs rapidly after 1–2 min of incubation (see Figure S4, Supporting Information) whereas aggregation still evolves more than 50 min after incubation (see Figure 2B-i and Figure S3C, Supporting Information). Such an observation is also consistent with a DLCA aggregation mechanism where aggregates have extended low density and linear structures with small numbers of contact points between particles.

Measurements of protein adsorption by DDM were also compared with those from the measurement of free protein by fluorescence spectroscopy after purification from the protein-NPs complex by centrifugation (see Experimental Section),

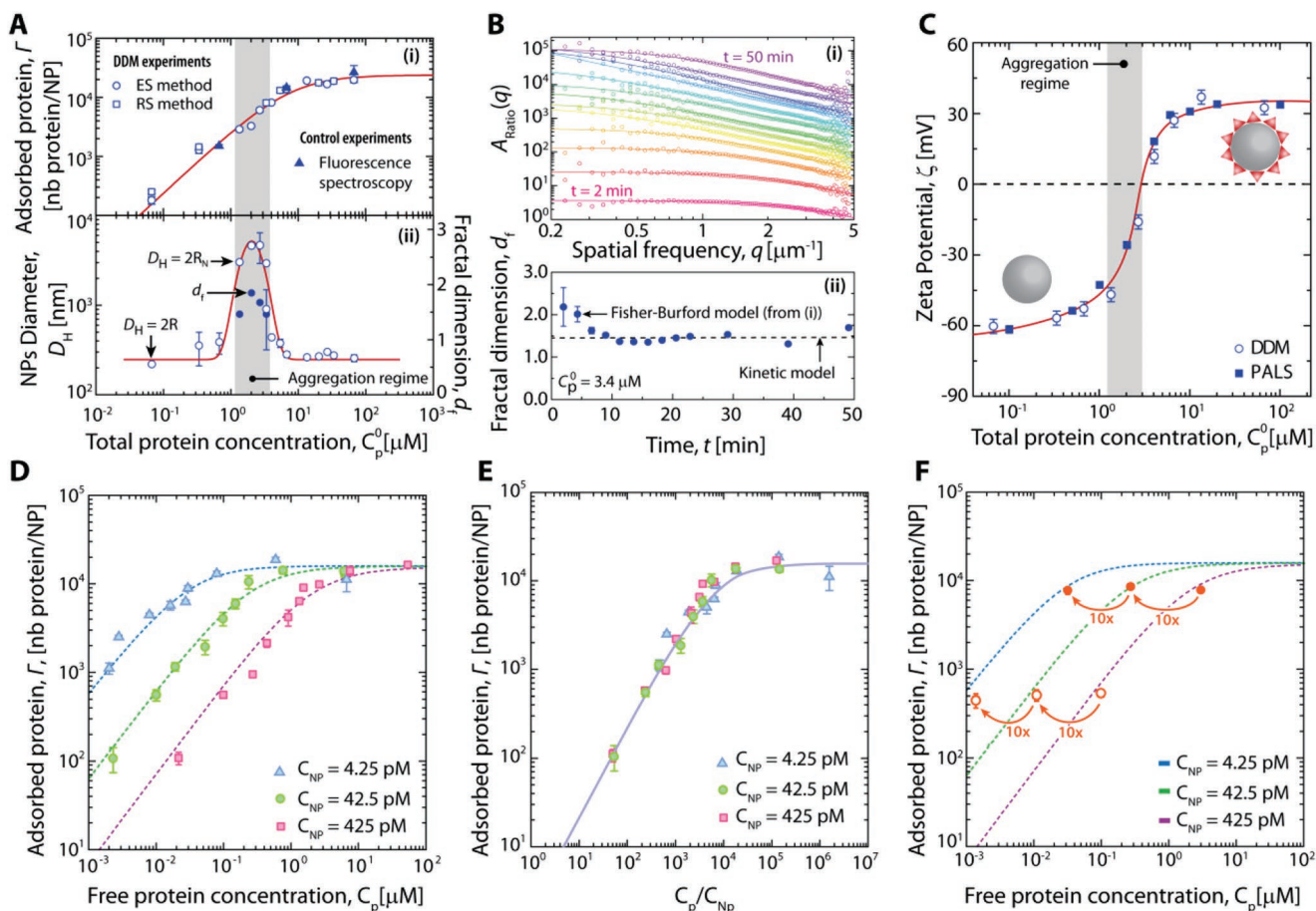


Figure 2. Quantification of LYZ on NPs, aggregation and fractal dimension. A) Adsorption isotherm and particle size measurement of PS NPs and LYZ mixtures. In the strong aggregation regime highlighted in gray, aggregates fractal dimension was quantified simultaneously by DDM after 20–30 min of incubation time. Measurements of protein adsorption (nb = number) by DDM are compared with the adsorption measurement from the quantification of free proteins by fluorescence spectroscopy after centrifugation. B) Protein adsorption triggers NPs aggregation. The aggregates fractal dimension, d_f , can be monitored by DDM. Curves in (i) are fits to the Fisher–Burford model from Equation (8). C) Quantification of adsorbed protein amounts by DDM shows excellent agreement with PALS providing an additional validation of the quantification method of DDM. The red line is a guide to the eye. D) Adsorption isotherms of LYZ on PS NPs at different particle concentrations were well described by the Hill adsorption model with a Hill coefficient $n = 1$ (dashed curves). E) Adsorption isotherms shown in D normalized by the concentration of NPs collapse into a single master curve and fitted by a modified Langmuir isotherm $\Gamma = \frac{\Gamma_{\text{max}} C_p / C_{\text{NP}}}{K_D + C_p / C_{\text{NP}}}$. F) Dilution of proteins/NPs mixture shows that the amount of adsorbed proteins after dilution is always consistent with the amount expected by an adsorption isotherm performed at the same dilution. Dashed lines are the fitted isotherms from (D). DDM data in (A–F) are averages of at least five acquisitions and the error bars represent one standard deviation.

shown in Figure 2A-i. The fluorescence linearity of proteins and the normalization process for intensity and aggregation can be visualized in Sections S5 and S6, Supporting Information. The excellent agreement between DDM and fluorescence spectroscopy measurements validates of the theoretical framework developed to measure protein adsorption.

Since LYZ is a positively charged protein adsorbing on a negatively charged PS particle, changes in the particle surface potential are expected to occur along the protein adsorption isotherm. In Figure 2C, measurements of the particles' zeta potential, ζ , performed via phase analysis light scattering (PALS), were compared to rescaled DDM measurements of Γ to map ζ measurements. This was achieved using the simple expression^[40] $\zeta = \left(\frac{\Gamma}{\Gamma_{\text{max}}} \right) \Delta\zeta + \zeta_{\text{NP}}$ where zeta potential change between the NPs and the protein $\Delta\zeta = \zeta_{\text{NP}} - \zeta_p = 100$ mV, the NPs zeta potential

$\zeta_{\text{NP}} = -65$ mV, $\Gamma_{\text{max}} = 18000$ where Γ and Γ_{max} were experimentally measured by DDM. The excellent agreement between the two methods represents an additional orthogonal validation of the DDM approach to accurately quantify Γ . As represented by the gray area in Figure 2A-ii, particle aggregation occurred at a protein surface coverage ranging between 2800 ± 200 and 8100 ± 100 LYZ/NPs (16% and 45%, respectively). At such surface coverage, the calculated NP effective surface indicates that full electrostatic screening has not occurred at the onset of aggregation. This result suggests that the aggregation process is not driven by Van der Waals forces but instead is likely governed by the bridging of the LYZ protein between two particles, “gluing” them strongly together and limiting self restructuration of the aggregate over time. Similar observations were reported by Moerz et al. for hemoglobin and gold NPs, suggesting that the phenomenon is extrapolable to other systems.^[39]

Using the validated methodology, affinity of lysozyme for NPs was evaluated at different NPs concentration, a parameter often forgotten in PC studies. Figure 2D shows three adsorption isotherms measured at three different $C_{NP} = 4.25, 42.5,$ and $425 \mu\text{M}$. Measurement of Γ by DDM at different free protein concentration C_p is well described by a Hill-type adsorption isotherm for all C_{NP} . The Hill-adsorption isotherm is derived from the equilibrium between a NP and n proteins P ($\text{NP} + n\text{P} \leftrightarrow \text{P}_n\text{NP}$) and can be written as^[41]

$$\frac{\Gamma}{\Gamma_{\max}} = \frac{(C_p)^n}{K_D + (C_p)^n} \quad (9)$$

where K_D is the dissociation constant of the P_nNP complex, Γ_{\max} is the maximum amount of protein that can adsorb onto NPs and n the Hill coefficient often described as the cooperativity index. In the case that $n = 1$, Equation (9) becomes the Langmuir isotherm. Here, experimental isotherms were all successfully modeled with the simplest form, $n = 1$. The free protein concentration was calculated based on DDM measurements of adsorbed protein Γ and total protein concentration C_p^0 from $C_p = C_p^0 - \Gamma C_{NP}$. Interestingly, a strong dependence of K_D with C_{NP} was observed, where K_D increased significantly from $0.028 \pm 0.006 \mu\text{M}$ to $2.263 \pm 0.418 \mu\text{M}$ for C_{NP} between 4.25 and $425 \mu\text{M}$. A value of $\Gamma_{\max} = 15\,800 \pm 1000$ proteins/NP was found for all three isotherms and could correspond to a protein monolayer at full coverage. The theoretical full coverage of a monolayer by LYZ on the NPs was estimated to be $\approx 16\,000$ proteins/NP considering that LYZ is a prolate ellipsoid of dimensions $2.8 \times 2.8 \times 5.0 \text{ nm}$ ^[42] and adsorbs at the positive electrostatic end of its structure^[43] with an effective surface footprint area of 7.84 nm^2 . Again, aggregation was observed for all NPs concentrations at a constant C_p/C_{NP} ratio (or Γ). However, the magnitude of the aggregation was strongly increasing with C_{NP} . The full extent of NPs aggregation and fractal dimension analysis is reported in Figure S7, Supporting Information.

Interestingly, normalizing the free protein concentration C_p by C_{NP} from the adsorption isotherm leads to a single master curve (see Figure 2E). This effect was previously reported by Milani et al., with the adsorption of transferrin on sulfonated polystyrene NPs, and was attributed to irreversible adsorption.^[11] The rescaling of the adsorption isotherm is in fact the consequence of a linear relationship between K_D and C_{NP} ($K_D \approx C_{NP}$, see Figure S8, Supporting Information) and has interesting consequences regarding the interpretation of reversible adsorption. Reversibility of protein adsorption is often tested by diluting a particle/protein mixture after protein adsorption equilibrium has been reached. In such situation, both C_p and C_{NP} decrease but their ratio C_p/C_{NP} remains constant. By monitoring Γ at each dilution, it can be seen in Figure 2F that its value does not change significantly, independently of the starting value of Γ on the adsorption isotherm (either close to the saturation plateau or in the low protein adsorption regime). Absence of desorption upon dilution challenges the very concept of adsorption isotherm (which describe a thermodynamic equilibrium) and has always been interpreted as a sign of irreversible adsorption.^[12,23] The observed linear relationship between K_D and C_{NP} provides a simple answer to this puzzle. Diluting the suspension in order to trigger desorption is causing a change in K_D

due to a change of C_{NP} and therefore modifies the adsorption isotherm as well. We illustrate this effect in Figure 2F where a dilution experiment was performed maintaining C_p/C_{NP} constant. In the figure, the different adsorption isotherms obtained in Figure 2D were represented as well as the values of Γ obtained at $C_{NP} = 425 \mu\text{M}$ and by diluting the protein/particle mixture by one order of magnitude multiple times. As can be seen, the Γ values obtained after dilution fall exactly on the isotherms obtained independently at the same corresponding C_{NP} . This correspondence between adsorption isotherms and dilution experiments confirms that dilution does not perturb the initial equilibrium and therefore adsorption is not a priori irreversible. This behavior was also observed with serum and BSA adsorption on PS NPs as shown later (Figure 3).

3.3. The Complex Adsorption Mechanism of Serum and BSA on PS NPs

DDM analysis can also provide insights on the formation of the PC in complex protein mixtures with minimal sample preparation. We used fluorescently labeled bovine serum and measured its adsorption isotherm on PS NPs with DDM. The obtained values of Γ shown in Figure 3 are effective quantity normalized by the molar mass of serum major constituent, BSA. These values were either obtained at constant C_{NP} or constant C_p^0 , and were therefore represented as a function of the ratio C_p/C_{NP} . Since the effective adsorbed amount Γ in serum is relative to BSA, values for Γ_{\max} , K_D , and aggregation regimes should be interpreted with this assumption in mind. The adsorption isotherm of bovine serum (expressed as effective BSA proteins per NP) exhibits two distinct adsorption regimes, clearly indicating changes in the PC composition depending on the total protein concentration. The adsorption isotherm was fitted with a two-step adsorption model based on the sum of two isotherms each similar to Equation (9) to extract apparent affinities and saturations (fitted parameters are summarized in Table 1). The first plateau was reached at $\Gamma_{\max-1} = 540 \pm 40$ protein per NP and the second plateau was reached at $\Gamma_{\max-2} = 4370 \pm 270$ protein per NP. The first adsorption step seems to correspond to the adsorption of high affinity ($K_{D-1} = 220 \pm 120$ protein/NP) large protein(s) such as fibrinogen, immunoglobulins, or some apolipoproteins. The second adsorption step can be ascribed to the adsorption of smaller protein(s) with weaker affinity ($K_{D-2} = 28\,500 \pm 5600$ protein per NP), a phenomenon reminiscent of the Vroman effect found at equilibrium.^[44] Simultaneous measurement of particle size showed that serum proteins induced strong aggregation of the NPs for $100 < C_p/C_{NP} < 2000$ (dark gray region in Figure 3A). Outside this range, particle diameter was still significantly larger than 200 nm indicating the presence of small aggregates (light gray region in Figure 3A) rather than multiple layers of proteins adsorbed on particles. Quantitative assessment of the fractal dimension of the aggregates was only possible in the strong aggregation regime due to limitations arising from the size of the particle aggregates. In this regime, an aggregate structure of $d_f = 2.13 \pm 0.13$ was found (see Figure S7, Supporting Information), which seems to be indicative of a reaction-limited colloid aggregation mechanism, producing more compact aggregates.^[33,38]

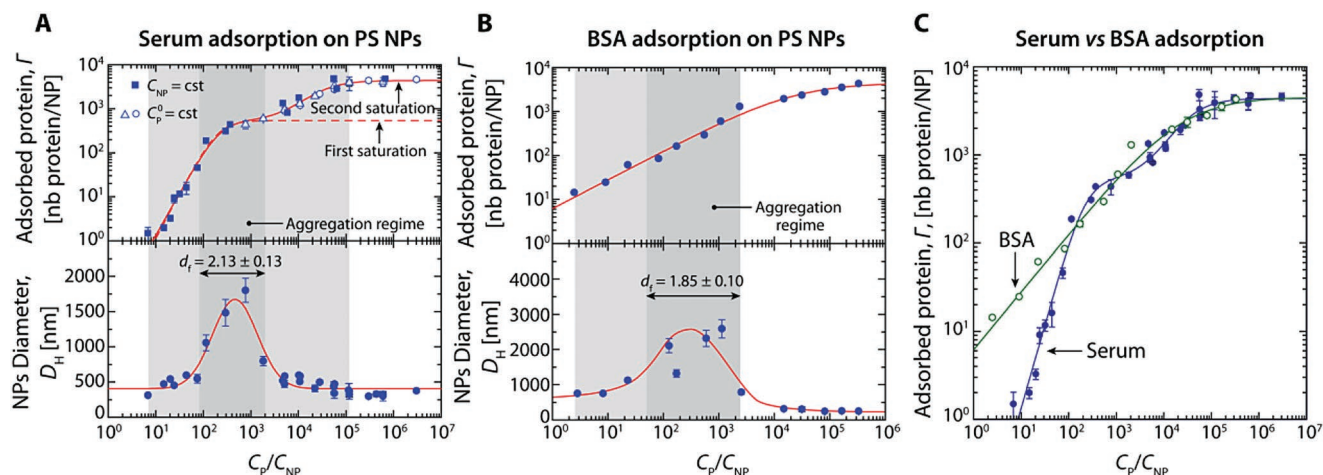


Figure 3. Quantification of adsorbed serum proteins. A) Adsorption isotherm, particle size, and fractal dimension of PS NPs/serum mixtures show multiple saturation plateaus reminiscent of significant variations in the PC composition along the isotherm. “Cst” represents the parameter kept constant in the adsorption experiment. B) The BSA adsorption isotherm can be described by the Hill isotherm and exhibits strong aggregation as all the other proteins tested. The 4-most dilute experiments ($100 > C_p/C_{NP}$) were tested at $C_{NP} = 425 \text{ } \mu\text{M}$, whereas all other experiments were tested at $C_{NP} = 42.5 \text{ } \mu\text{M}$. C) Superposition of the serum and BSA adsorption isotherms shows strong overlapping in the high concentration region. In that region, the serum PC is expected to be largely composed of BSA. The lines in the upper panels are fits to a sum of two expressions of Equation (9) in (A) and to Equation (9) in (B) that were also re-used in (C). The lines in the lower panels for size measurements are guide to the eye. DDM data in the figure are averages of at least five videos and error bars represent one standard deviation.

A large body of proteomic studies of the protein corona of PS NPs, typically performed *ex situ*, have shown that albumin is one of the major component,^[3,45] but not systematically.^[2,8] Other protein are often found in large proportion, notably fibrinogen, complement proteins, immunoglobulins, and apolipoproteins. However, their absolute composition varies significantly across studies. To gain more insights into the composition of the serum PC just described, we measured in a separate experiment the adsorption isotherm of BSA on PS NPs (Figure 3B). The isotherm could be fitted with Equation (9) and fitted parameters are summarized in Table 1 and compared to those obtained with serum. Given that the albumin has a structure of an equilateral triangular prism, with sides of $\approx 8 \text{ nm}$ and a thickness of $\approx 3 \text{ nm}$ ^[46], the number of BSA to reach the full coverage of a monolayer can be estimated. With the consideration that BSA would adopt a side-on orientation (footprint of 277 nm^2) on PS NPs of available surface area of $1.26 \times 10^5 \text{ nm}^2$, the theoretical maximum coverage $\Gamma_{\text{max}} = 4540 \text{ BSA/NP}$ is in perfect agreement with our measurements of $\Gamma_{\text{max}} = 4500 \pm 600 \text{ BSA/NP}$. Note that the anti-cooperative behavior of BSA adsorption of $n = 0.66 \pm 0.07$ is also in agreement with several other reports for albumin adsorption (on negatively charged NPs), irrespective of the size or chemical composition of the NPs.^[22,23,47,48]

BSA adsorption induced strong particle aggregation between $50 < C_p/C_{NP} < 2200$, a range that is similar to serum (see Figure 3A). Interestingly, the fractal dimension measured in the strong aggregation regime was lower compared to serum and equal to $d_f = 1.85 \pm 0.10$, indicative of a DLCA mechanism (see Figure S7, Supporting Information).

In Figure 3C, both serum and BSA adsorption isotherms overlap in the high protein concentration range, where the second saturation regime of the serum isotherm was observed ($C_p/C_{NP} > 10^3$). In this regime both isotherms exhibited a similar $K_D \approx 25000$ proteins per NPs. Such overlapping between both isotherms indicates that, in this adsorption regime (high number of proteins per NPs), the composition of the PC in serum is largely dominated by albumin (or by proteins with similar molar mass and affinity) as both final saturation states Γ_{max} approach ≈ 4500 proteins/NPs. On the other hand, for $C_p/C_{NP} < 10^3$, BSA isotherm presents a higher amount of adsorbed proteins compared to serum. Because of the complex composition of serum, it is likely that in this adsorption regime the PC composition shifted from BSA to larger proteins with stronger affinities. This was also reflected in the difference of aggregates structure and mechanism, where BSA generated a loose structure from a diffusion-limited mechanism (DLCA)

Table 1. Summary of serum and BSA measurements.

Protein	Γ_{max} [protein per NP]	Affinity measurement			Aggregation
		K_D [protein per NP]	K_D [nM] ^{a)}	n	d_f
Serum (first process)	540 ± 40	220 ± 120	9.4 ± 5.1	1.97 ± 0.70	2.13 ± 0.13
Serum (second process)	4370 ± 270	28 500 ± 5600	1210 ± 240	1.26 ± 0.27	
BSA	4500 ± 600	22700 ± 12000	960 ± 510	0.66 ± 0.07	1.85 ± 0.10

^{a)}Dissociation constant (K_D) calculated for a NP concentration of $42.5 \text{ } \mu\text{M}$.

compared to the more compact structure produced by reaction-limited aggregation (RLCA) for serum ($d_f(\text{serum}) > d_f(\text{BSA})$). As demonstrated, aggregation is triggered by the adsorption of the proteins, hence a change in the aggregation mechanism is likely to indicate a change in the type of proteins adsorbed. In the very low concentration regime, $C_p/C_{NP} = 10$, the adsorption of BSA is more than an order of magnitude higher than serum, indicating that the adsorbed proteins from serum have a very different affinity and interaction with the NPs compared to BSA. Indeed, the difference between the Hill coefficients of serum $n = 1.97 \pm 0.70$ and BSA $n = 0.66 \pm 0.07$ obtained in the low concentration regime also suggests a different binding mechanism. Similar observations were made for the adsorption of BSA and serum on negatively charged quantum dots. Wang et al., reported Hill coefficients of $n = 1.8 \pm 0.2$ for serum and $n = 0.6 \pm 0.1$ human serum albumin (HSA)^[23] corroborating our observations. Furthermore, the ratio between K_D measured in HSA versus serum in their experiments ($K_{D\text{-HSA}}/K_{D\text{-serum}} \approx 90$) is also in agreement with our experiments ($K_{D\text{-BSA}}/K_{D\text{-serum}} \approx 100$). Altogether these experiments confirm that the PC composition is strongly dependent on the serum concentration used in the suspending media. This phenomenon observed at equilibrium is also known as the general Vroman effect. It was first reported on flat surfaces^[44] but only few studies have shown some evidence of this effect on NPs.^[49]

3.4. Monitoring the PC Exchange Kinetics In Vitro

The versatility of the DDM setup allows to perform time-dependent experiments of protein adsorption in different settings. In Figure 4A we show adsorption kinetic curves of LYZ

on PS particles in three different experimental configurations. The first two configurations are competitive assays where NPs were precoated with either labeled (Figure 4A-i) or unlabeled (Figure 4A-ii) LYZ and exposed to a medium containing the corresponding unlabeled or labeled protein. The results of these two tests showed the exchange of the preadsorbed proteins with proteins from the medium and confirmed the reversibility of the adsorption process, even for a strongly adsorbing protein such as LYZ, in agreement with the earlier observations from the adsorption isotherm and the dilution experiment. A simple exponential decay model, based on a pseudo-first order kinetics,^[15] was used to model both adsorption and desorption experiments. Because the total protein concentration (labeled and unlabeled) was constant in both experiments, it was expected that both exchange rate constants k of adsorption and desorption match. We confirmed this was indeed the case as the measured rate constants for adsorption $k = 0.020 \pm 0.002 \text{ min}^{-1}$ was in fair agreement with the rate constants for desorption $k = 0.030 \pm 0.005 \text{ min}^{-1}$ considering the experimental error. Interestingly, the competition kinetics is significantly much slower ($>30\times$) than the adsorption kinetics of free LYZ (see Figure S4, Supporting Information). This suggests that upon first contact with a biological fluid, NPs get covered with a layer of proteins within seconds, while competing proteins (slower or further away from the NP) may take from minutes to hours to displace previously adsorbed proteins and reach equilibrium. However, it was also expected that both final equilibrium would converge toward a common value of proteins/NP, though experiments shows that the expected “complete re-equilibrium” was not achieved during the experimental time-window.

The third assay is a dilution assay where precoated particles with labeled LYZ were mixed with uncoated nanoparticles. The

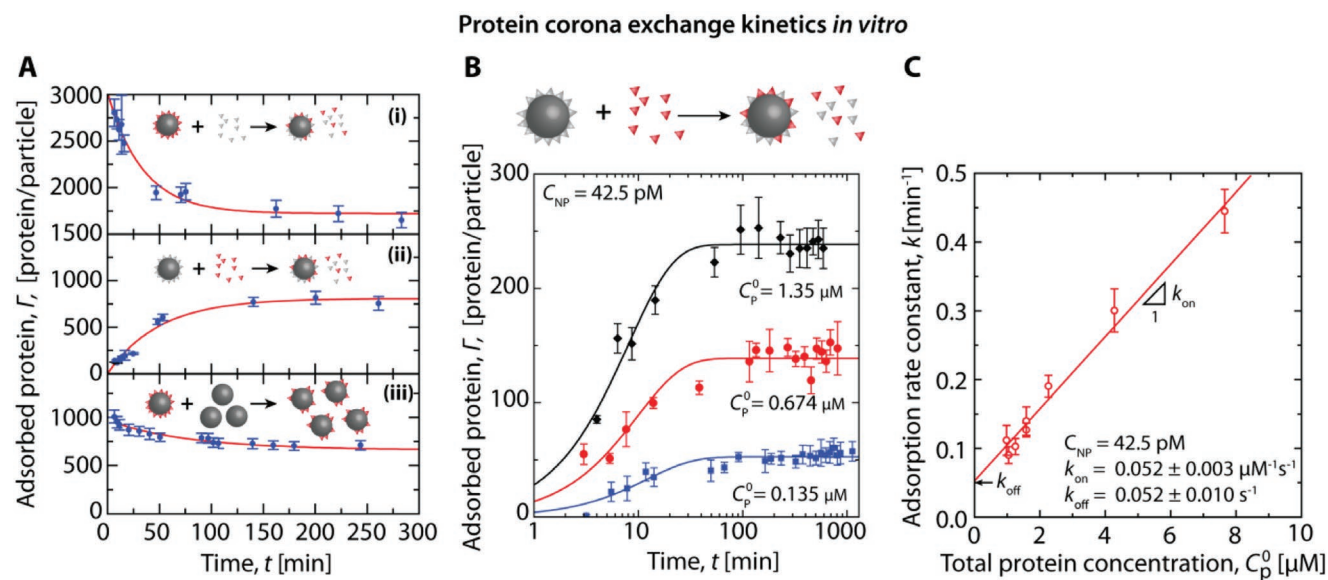


Figure 4. Kinetics of the PC formation in vitro. A) Protein exchange at the PC interface can be performed by DDM in different configurations to test the reversibility of protein adsorption. Changes in adsorbed labeled protein is modeled using $\Gamma(t) = \Gamma_{eq} + \Delta\Gamma \exp(-kt)$, with free parameters Γ_{eq} and $\Delta\Gamma$ are the adsorbed amount at equilibrium and the change of the adsorbed amount of labeled proteins, respectively. B) Monitoring of protein exchange at the PC interface in presence of lysozyme at different concentrations of labeled proteins. C) Evolution of the adsorption rate constant with the protein content allows to extract adsorption constants. The red line is a linear fit to the experimental data points, and the error bars are the parameters' fitting standard errors. DDM data in (A) and (B) represent one measurement and the error bars represent the standard deviation of the $\langle A_{ratio} \rangle_q$.

concentration of proteins used for this experiment was below the saturation limit of the particles, therefore almost all the proteins were adsorbed and very few were still free in the medium ($\approx 10\%$). Addition of bare particles triggered a decrease in the amount of proteins per particle (Figure 4A-iii), indicative of a slow redistribution of the proteins throughout the NP suspension. After 200 min, a new equilibrium was reached at $\Gamma = 720$ proteins per NP, which was still higher than the expected value if complete and homogeneous redistribution of the proteins had occurred (450 proteins per NP). Even after 150 min, it appears that the initially bare NPs introduced in the suspension still had a lower amount of adsorbed proteins compared to the NPs that were precoated. Interestingly, the expected “complete re-equilibrium” was not achieved within the experimental observation time for any experiment. This curious behavior might suggest that even though protein adsorption is a dynamic and reversible process, “memory effects” might produce inhomogeneities in PC composition, as similarly reported by Vilanova et al.,^[50] altering the equilibrium state over time.

Quantitatively assessing the exchange rate of proteins at different fluorescent protein concentration can also yield the equilibrium constant. Using the same design as in Figure 4A-ii, NPs precoated with unlabeled LYZ (at $\Gamma = \Gamma_{\max}$) were incubated with a solution of LYZ-RITC and their exchange was followed by DDM. In Figure 4B the number of labeled proteins adsorbed per NP over time is shown. The kinetics of the exchange between labeled and unlabeled proteins is analyzed as in the previous experiment to extract the exchange rate constant, k . As previously shown, k is related to the adsorption and desorption rates constants, k_{on} and k_{off} , via the expression^[22] $k = k_{\text{off}} + C_{\text{p}}^0 k_{\text{on}}$. Figure 4C shows the results of this analysis for $C_{\text{NP}} = 42.5 \text{ pM}$. The dissociation constant measured via the adsorption isotherm is related to the ratio of the kinetics constants by $K_{\text{D}} = k_{\text{off}}/k_{\text{on}}$. A dissociation constant of $K_{\text{D}} = 1.0 \pm 0.3 \text{ }\mu\text{M}$ was obtained from the exchange kinetics assay as presented in Figure 4B,C, less than an order of magnitude difference with $K_{\text{D}} = 0.26 \pm 0.05 \text{ }\mu\text{M}$ measured from the adsorption isotherms shown in Figure 2D. The difference between adsorption kinetics and equilibrium values may arise from a slight difference in affinity that was observed between the labeled and the unlabeled LYZ, also observed in other studies.^[51] Furthermore, the memory effect observed in previous experiments may also influence the agreement between both the kinetics and the equilibrium experiments. Hence, the experimental values may not fully agree, but kinetics and equilibrium approaches confirm that the lysozyme adsorption at the surface of the NP is a reversible process. However, that process is presumably not captured by classical “Langmuirian” adsorption models and will require finer details of the adsorption mechanism to account for the affinity dependence on CNP in equilibrium experiments and the memory effects in kinetics experiments.

3.5. Monitoring In Vivo the PC Exchange Kinetics in Zebrafish Larvae

These in vitro experiments demonstrate kinetic and thermodynamic properties of the PC formation and more questions arise regarding the PC in more complex, yet real, environments.

Indeed, some reports have suggested that in vivo the PC composition evolves with time,^[3,52] while other reports have suggested that the PC constitutes the fingerprint of the NPs, its biological identity.^[19] To provide more insights into PC dynamics in vivo, we used DDM to follow the composition of the PC in zebrafish larvae 48 h post fertilization (hpf).

The zebrafish larvae constitute a powerful model for PC studies using DDM since the transparency of the larvae allows intravital imaging. NPs precoated with labeled serum proteins were injected in the bloodstream of 48 h post-fertilization larvae and imaged in the caudal venous plexus (CVP) (Figure 5A). The CVP has a characteristic dense and tortuous capillary network through which the bloodstream flow speed is far slower (average speed of $\approx 30 \text{ }\mu\text{m s}^{-1}$) than the flow in the main artery (average speed $>100 \text{ }\mu\text{m s}^{-1}$), as estimated by video imaging. The low flow speed facilitates the capture of any circulating foreign bodies such as NPs by either macrophage cells on the lining of the subcaudal venous capillaries or by vascular endothelial cells, a dominant mechanism found in the clearance of “hard nanomaterials” by the liver.^[53] Indeed, CVP is often compared to hepatic sinusoids, which are composed of liver sinusoidal endothelial cells (LSECs) and Kupffer cells.^[54,55] The vascular endothelial cells in the CVP area are functionally equivalent to LSECs (i.e., cells having scavenger receptors on their surface).^[55] Our experiments highlighted an accumulation of NPs over time in the CVP region (see Figure S9, Supporting Information) which is in agreement with previous findings.^[55]

Only a few minutes after NPs injection, NPs appeared as “immobilized” in the CVP on the lining of the capillaries in the form of small patches (Figure 5A-i). Circulating NPs were scarce and did not contribute to the DDM signal amplitude of immobilized NPs $A_{\text{NP}}(q)$ as their ballistic motion was many orders of magnitude faster than immobilized NPs so that their contribution have likely been captured in $B^*(q)$ instead. Besides being captured by endothelial cells, we found NPs still exhibited diffusive Brownian motion at the surface of the blood vessels. As shown in Figure 5B, the dependence of the ISF with q can be normalized into a single master curve when plotted against πq^2 , to highlight the diffusive nature of the measured dynamics. This analysis allowed to extract the diffusion coefficient, D , of the NPs. The calculated values were three orders of magnitudes lower for immobilized NPs ($D_{\text{f}} = 0.00168 \text{ }\mu\text{m}^2 \text{ s}^{-1}$) compared to NPs diffusing in water ($D_{\text{w}} = 2.1 \text{ }\mu\text{m}^2 \text{ s}^{-1}$, at $21 \text{ }^\circ\text{C}$), see Figure 5B-iii. Recently, Kwapiszewska et al. have shown that the effective viscosity, $\eta_{\text{eff}} = D_{\text{w}}/D_{\text{f}}$ for NPs of similar size located in the cytosol of different cell lines is at least two orders of magnitude smaller than our measurements for the immobilized NPs.^[56] Several studies have also shown that cell membrane can be considered as a newtonian fluid^[57] with a viscosity two to three orders of magnitude higher than water,^[58] in contrast to the rheologically complex cytosol,^[59] which is in line with our observations. Based on these observations, our results therefore support the notion that the NPs were located at the surface of the capillary lining to which they adhered most probably via receptor-mediated interactions as their accumulation were predominantly in the CVP. Therefore, their dynamics at the cell surface is expected to be coupled to the dynamics of the receptor in the plasmatic cell membrane which is dominated by Brownian motion (i.e., diffusive behavior^[60]).

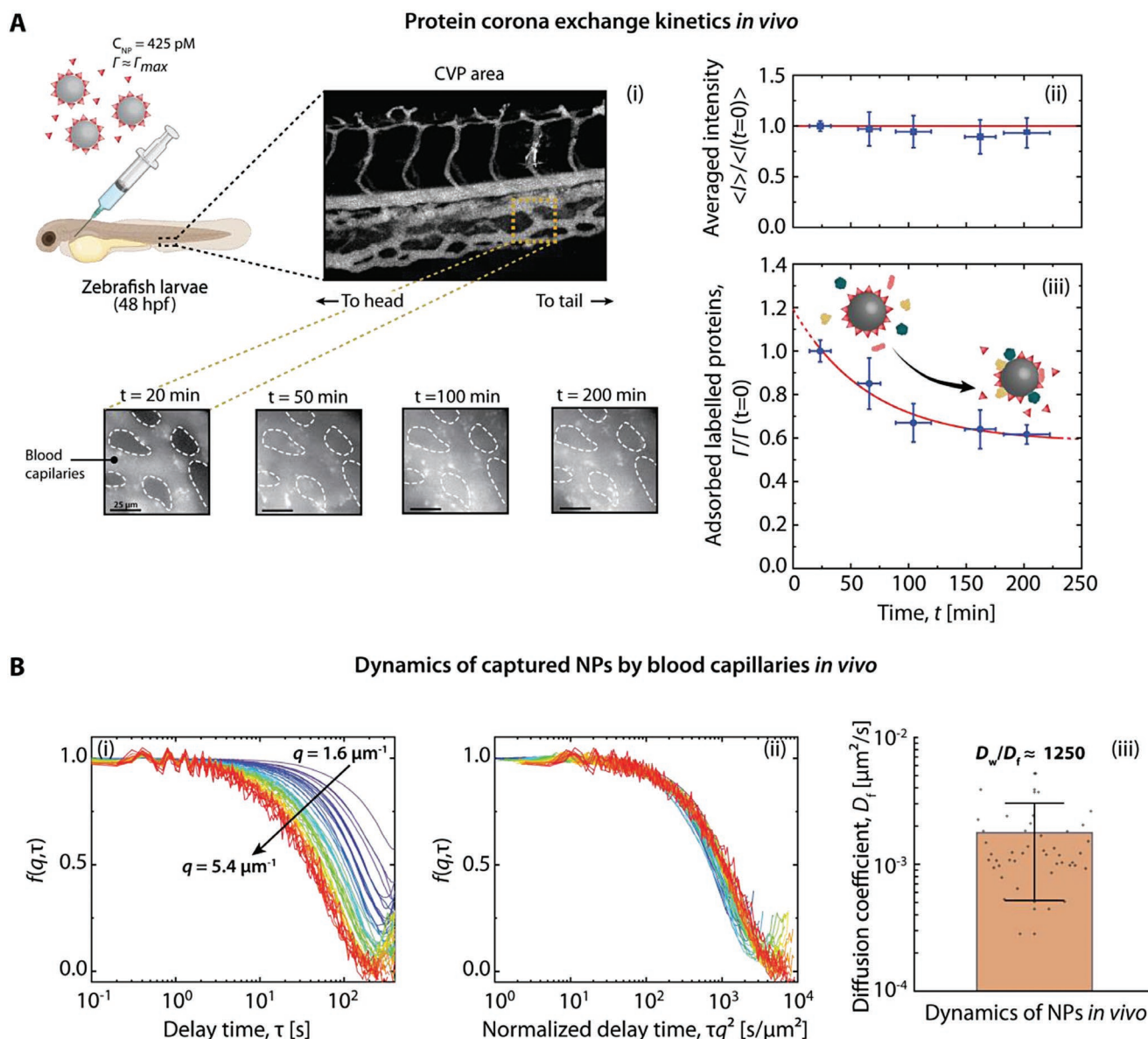


Figure 5. In vivo evaluation of the PC kinetics in zebrafish larvae. A) Imaging of NPs in the zebrafish larva (48 hpf) post injection show rapid and stable immobilization of the NPs on the lining of the blood capillaries of the subcaudal region (i). In the right panels, the normalized average fluorescence intensity captured by the camera (ii) and the time evolution of the PC composition of NPs immobilized in the CVP area of the zebrafish larvae in vivo (iii). Data in (ii) and (iii) are cluster averages over $n = 3$ independent experiments (see Figure S10, Supporting Information) and the error bars their associated standard deviation. B) Dynamics of the immobilized NPs show a single process on the whole range of spatial frequency (i) where its normalization by τq^2 leads to a master curve demonstrating the diffusive nature of the motion of captured NPs (ii). The extracted coefficient of the immobilized NPs for many measurements (shown in the right panel) is consistent with the NPs being adsorbed at the cells surface but not internalized (iii). Error bars denote three standard errors to the data distribution.

After their capture, NPs dynamics was followed by DDM and the amount of adsorbed proteins was measured normalized to the first measurement as previously described (Equations (4) and (6)). As can be seen in the different snapshots shown in Figure 5A-i, the fluorescence intensity was initially concentrated in the NPs patches and inside the blood capillaries. Over time, it invaded intercapillary regions, probably indicating a fast diffusion of free fluorescent proteins outside of the blood capillaries, whereas NPs remained confined within the bloodstream. Some of the free proteins may be the

result of desorption, but NPs were injected along with a large free fraction of proteins as well. The protein exchange kinetics at the PC interface exhibited a single exponential decay over 3 h of observation (Figure 5A-iii). Three different zebrafish larvae were included in the analysis and data were clustered for clarity (see Figure S10, Supporting Information, for individual measurements). In the region of interest, no significant variation of the total fluorescence intensity was observed over the time of experiment (Figure 5A-ii), confirming that the number of captured particles did not increase during

image acquisition. The decrease in signal intensity can be thus solely attributed to the desorption of fluorescent proteins. Over this time window (≈ 3 h), the number of labeled proteins pre-adsorbed on the NPs decreased by 40%, indicating a slow exchange of characteristic time $\tau_{\text{desorption}} = 67 \pm 28$ min with unlabeled circulating blood proteins. It is important to note that the observed decay was monitored post-immobilization of the NPs and therefore does not provide any information regarding the PC dynamics of circulating NPs immediately after injection. Also, the rate at which NPs were immobilized in the CVP ($\tau < 10$ min) was faster than the rate the proteins were exchanged in this experiment. Therefore, it is unlikely that the change of the PC triggered by the adsorption of circulating zebrafish larvae proteins had any effect on the behavior of the NPs. In vivo serum protein exchange at the surface of the NPs was also not complete after 3 h of experimental observation. This observation is analogous to the in vitro observation of LYZ, where a fraction of proteins appears to exhibit no exchange with the surrounding biological medium, a likely manifestation of the “biological memory effect,”^[61] or the so-called “hardening” of the PC.^[19,20] These in vitro and in vivo experiments clearly show that this effect is a unique feature of the PC and is observable in single protein solutions and complex mixtures as well.

4. Conclusion

Using a series of in vitro and in vivo assays, we have shown that DDM is a powerful technique to study proteins–particles interactions in situ and quantitatively. In vitro, protein adsorption on NPs was quantitatively assessed even in presence of NPs aggregation, which was systematically observed for all the proteins and mixture of proteins (serum) studied. The developed framework quantitatively characterized the aggregates structure via its fractal dimension. However, this framework is only valid for isotropic (spherical) NPs, but would require modifications for highly anisotropic NPs, for example nanorods, fibres, and nanosheets.

Using DDM, it was possible to measure the affinity between proteins and NPs. Interestingly, the apparent affinity between LYZ and PS NPs was observed to change with concentration of NPs. No protein desorption was observed from dilution experiments, whereas competition experiments clearly demonstrated the reversibility of the adsorption. Here, we insist protein adsorption on NPs may not be a typical “Langmuirian” adsorption process, hence the C_{NP} effect on the affinity. This concentration scaling of the adsorption could have severe repercussions on reproducibility and biodistribution if not considered. For instance, a recent study by Ouyang et al., demonstrated that the number and concentration of injected NPs is playing a major role over targeting efficiency and tumor delivery, a parameter not often emphasized by studies.^[62] Accordingly, this work reiterates the importance of understanding the effects of NPs concentration in nanomedicine.

Our methodology also contributed to observe a phenomenon reminiscent of the Vroman effect at equilibrium from the changes in the PC composition contingent to the serum concentration. The most reasonable interpretation of the

experimental data is consistent with reports on planar surfaces,^[44] where large proteins are adsorbed at “high dilution” (low $C_{\text{P}}/C_{\text{NP}}$) while albumins or other proteins of similar molar mass and affinities are predominant at higher serum concentration (high $C_{\text{P}}/C_{\text{NP}}$).

Also, it is important to remember that for all protein-NPs systems and conditions tested, monolayers of adsorbed proteins were observed. Indeed, the number of proteins per NPs measured by DDM at saturation (Γ_{max}) for all proteins evaluated was in reasonably good agreement with the formation of a monolayer of proteins based on their 3D structures. These results agree well with reports from Nienhaus’ group,^[12,22–24,48,63] where their evaluation of the PC thickness mostly led to the conclusion of monolayers. Moreover, it was demonstrated that the monolayer is the most prevalent structure of the PC, but that multilayer could be favored under specific circumstances related to the NP physicochemical nature (e.g., size and type of NP material).^[15]

Finally, the methodological approach validated for in vitro experiments was adapted and used to study the PC formation and composition dynamics in the zebrafish larvae. Those in vivo experiments demonstrated the partial exchange of proteins in the PC that was also observed in vitro. The existence of a long-lived protein layer which exhibits very slow exchange dynamics is consistent with the so-called biological memory effect and reveals that the PC is long-lived, but dynamic in nature.

We emphasize that the nature of DDM methodology makes a powerful alliance of quantitative video analysis and visual inspection of video imaging. From its successful transition to in vivo systems, we aim of moving toward a better quantification of nanomedicine behavior in living organisms.

5. Experimental Section

Materials: Plain PS NPs of $R = 110$ nm, $R = 30$ nm (Duke Standards, Thermofisher) and plain PS NPs of $R = 100$ nm (Polysciences) were used after 1-week dialysis (SpectraPor membrane, 50 kDa MWCO) in MilliQ water to remove any potential traces of surfactant. Fluorescent PS NPs of $R = 110$ nm (Polysciences) were used after a purification step by exclusion chromatography. LYZ (Sigma-Aldrich), BSA (Sigma-Aldrich), serum proteins (Gibco, Thermofisher), and the fluorescent labeling agent, RITC (Sigma-Aldrich), were all used as is.

Protein Labeling: The labeling procedure of proteins was based on published reports.^[17,64] Serum proteins from fetal bovine serum (FBS), BSA, and LYZ were labeled with rhodamine B isothiocyanate (RITC) using a molar ratio of 5:1 RITC per equivalent proteins (assuming a concentration of proteins of 40 mg mL⁻¹ BSA equivalent for serum). Proteins were mixed with carbonate buffer (NaHCO₃ 0.2 M, pH = 8.35) to which RITC dissolved in 10% v/v DMSO was added. The coupling reaction was carried at room temperature for 1 h under gentle stirring and then transferred at 4 °C overnight. The resulting solution was dialyzed (SpectraPor membrane, 1000 Da MWCO) against PBS for 3 h and then centrifuged (30 min at 10000g) to remove any aggregates. The sample was further purified on Sephadex G-20 columns (GE Healthcare, PD-10) to remove any excess of free RITC. Aliquots were kept at -20 °C until use. For LYZ, protein concentrations in the final stock solution were determined by UV–vis spectrophotometry. Serum proteins and BSA concentrations were measured based on BCA assays, Pierce protein assay working at 660 nm (Thermo Scientific). Labeling efficiencies were determined based on the spectrophotometric absorbance at 554 nm of the fluorescent protein solutions. The resulting

labeling efficiencies were ≈40% for LYZ and ≈80% for both serum and BSA.

Fluorescence Spectroscopy Quantification: A calibration curve spanning from 0.017 to 3.7 μm was used to quantify adsorption of LYZ-RITC on PS NPs. The fluorescence was quantified using a microplate reader (TECAN Spark) using an excitation wavelength of 545 nm and an emission wavelength of 590 nm. For each sample, PS NPs incubated with LYZ-RITC were purified by one centrifugation (30 min at 20 000 × g). Supernatants (50 μL) were mixed with a solution of 10 mM HEPES (50 μL) and then distributed in a 96-well plate for fluorescence measurement.

Differential Dynamic Microscopy: An upright microscope (Olympus BX61, Japan) equipped with a high-speed camera (Hamamatsu OrcaFlash 4.0 V3, Japan) was used for the acquisition of videos. Videos were recorded using fluorescence imaging using 20 × objective (Olympus UPlanFL N, NA = 0.5), at a frame rate ranging from 10 to 100 frames per second, with an image binning of 1 × 1 or 4 × 4, and within a region of interest of 512 × 512 pixels. Fluorescence illumination was produced by a mercury burner and double band pass filters (FITC + TRITC) were installed. A neutral density filter blocking 94% of the incoming intensity was also installed to adjust the fluorescence intensity and minimize photobleaching. These parameters were adjusted to maximize the signal intensity and to fully capture the particle dynamics over an adequate *q* range and timescale for each experiment. Images were recorded on glass capillaries (Vitrocom, Canada) of 0.4 mm thickness filled with nanoparticle suspension (≈180 μL) and sealed using petroleum jelly. Videos were recorded at five different positions for each capillary and results were averaged over these five positions. Prior to video acquisition, proteins and particles were mixed before injection in capillaries. Adsorption experiments were carried at different protein (≈10⁻³ to 10² μM) and particle (4.25–425 μm) concentrations in different incubation media. For serum and BSA, adsorption experiments were performed in PBS (Gibco, Thermofisher), whereas for lysozyme experiments were performed in non-saline buffer (HEPES pH = 7.4).

Zeta Potential Measurement: Zeta potential measurements were performed using PALS analysis on a Zetasizer NanoZS device (Malvern Instruments, UK). Measurements were performed at a single scattering angle $\theta = 173^\circ$, at temperature of 21 °C and NaCl concentration of 4 mM.

DDM In Vivo: Experiments in zebrafish larvae were performed in compliance with the guidelines of the Canadian Council for Animal Care and following procedures defined in protocol #2005-03 issued to Pr SA Patten and approved by the local ethical committee. Wild-type zebrafish, Tupfel long-fin (TL) strain, were maintained at 28 °C and kept under a 12/12 h light/dark cycle at the animal facility of the Centre National de Biologie Expérimentale (CNBE), Laval, Canada. PTU was added to fertilized eggs at 24 h post-fertilization (hpf) to prevent larvae pigmentation. NPs were injected in 48 hpf larvae as previously described.^[65] Briefly, 48 hpf larvae were placed on the side in low melting point Agarose in 35 mm glass bottom Petri dishes. Zebrafish larvae were injected using a micropipette (10 cm Borosilicate Glass Micropipette with filament, Sutter Instrument, USA) pulled on a Micropipette Puller Model P97 (Sutter Instrument, USA). The injection in the duct of Cuvier was controlled with a nanoinjector FemtoJet 4i (Eppendorf, USA). Volume injected was 4 nL and the NPs concentration was set at 425 μM and the serum protein concentration at 13 μM equivalent BSA. Videos of NPs dynamics inside the blood circulation were recorded immediately after particle injections in larvae using a Zeiss inverted microscope equipped with a Plan-Apochromat 20x/0.8 M27 objective, a LED illumination lamp (X-cite 120LED, Excelitas Technologies) set close to minimum intensities (1–5%) and mounted with a Hamamatsu Orca Flash4.0 V3 camera. Camera frame rate was set between 10–30 fps depending on the experimental requirement.

Statistical Analysis: Pre-processing of data was performed following the theory section from Equations (1)–(6) for unaggregated samples and Equations (1)–(8) for aggregated samples. Otherwise specified, all the data points presented in the manuscript are an average of at least five

independent measurements and their associated error bars represents one standard deviation. Curves fitted to data points were obtained via non-linear regression analysis, performed with Origin Pro 2021.

Supporting Information

Supporting Information is available from the Wiley Online Library or from the author.

Acknowledgements

Charlotte Zaouter (Pr SA Patten laboratory) is acknowledged for her help with zebrafish husbandry. The authors would also like to thank Jessy Tremblay, coordinator of the cytometry and microscopy platform at the INRS Center Armand-Frappier Santé Biotechnologie, for his help with the in vivo microscopy experiments. P.L.L. thanks NSERC/CRSNG (Government of Canada) and faculty of pharmacy (UdeM) for Ph.D. scholarship. J.M.R. thanks NSERC/CRSNG (Government of Canada) for postdoctoral fellowship. This research was undertaken thanks, in part, to funding from the Canada First Research Excellence Fund through the TransMedTech Institute (postdoctoral fellowships given to J.M.R. and M.L.G., doctoral grant to S.S.). X.B. is grateful to the Canada Research Chair funding program and NSERC (Discovery grant and NOVA) for financial support.

Conflict of Interest

The authors declare no conflict of interest.

Data Availability Statement

The data that support the findings of this study are available from the corresponding author upon reasonable request.

Keywords

bio-nano interactions, differential dynamic microscopy, in vivo quantification, protein corona, Vroman effect

Received: April 13, 2022

Revised: July 23, 2022

Published online: August 16, 2022

- [1] a) D. Walczyk, F. B. Bombelli, M. P. Monopoli, I. Lynch, K. A. Dawson, *J. Am. Chem. Soc.* **2010**, *132*, 5761; b) M. P. Monopoli, C. Aberg, A. Salvati, K. A. Dawson, *Nat. Nanotechnol.* **2012**, *7*, 779; c) D. Docter, D. Westmeier, M. Markiewicz, S. Stolte, S. K. Knauer, R. H. Stauber, *Chem. Soc. Rev.* **2015**, *44*, 6094.
- [2] M. P. Monopoli, D. Walczyk, A. Campbell, G. Elia, I. Lynch, F. B. Bombelli, K. A. Dawson, *J. Am. Chem. Soc.* **2011**, *133*, 2525.
- [3] S. Tenzer, D. Docter, J. Kuharev, A. Musyanovych, V. Fetz, R. Hecht, F. Schlenk, D. Fischer, K. Kiouptsi, C. Reinhardt, K. Landfester, H. Schild, M. Maskos, S. K. Knauer, R. H. Stauber, *Nat. Nanotechnol.* **2013**, *8*, 772.
- [4] N. Bertrand, P. Grenier, M. Mahmoudi, E. M. Lima, E. A. Appel, F. Dormont, J. M. Lim, R. Karnik, R. Langer, O. C. Farokhzad, *Nat. Commun.* **2017**, *8*, 777.

- [5] H. R. Kim, S. Gil, K. Andrieux, V. Nicolas, M. Appel, H. Chacun, D. Desmaële, F. Taran, D. Geogin, P. Couvreur, *Cell. Mol. Life Sci.* **2007**, *64*, 356.
- [6] Y. Dong, K. T. Love, J. R. Dorkin, S. Sirirungruang, Y. Zhang, D. Chen, R. L. Bogorad, H. Yin, Y. Chen, A. J. Vegas, C. A. Alabi, G. Sahay, K. T. Olejnik, W. Wang, A. Schroeder, A. K. R. Lytton-Jean, D. J. Siegwart, A. Akinc, C. Barnes, S. A. Barros, M. Carioto, K. Fitzgerald, J. Hettinger, V. Kumar, T. I. Novobrantseva, J. Qin, W. Querbes, V. Kotliansky, R. Langer, D. G. Anderson, *Proc. Natl. Acad. Sci. USA* **2014**, *111*, 3955.
- [7] S. Schöttler, G. Becker, S. Winzen, T. Steinbach, K. Mohr, K. Landfester, V. Mailänder, F. R. Wurm, *Nat. Nanotechnol.* **2016**, *11*, 372.
- [8] S. Ritz, S. Schottler, N. Kotman, G. Baier, A. Musyanovych, J. Kuharev, K. Landfester, H. Schild, O. Jahn, S. Tenzer, V. Mailänder, *Biomacromolecules* **2015**, *16*, 1311.
- [9] C. D. Walkey, J. B. Olsen, F. Song, R. Liu, H. Guo, D. W. Olsen, Y. Cohen, A. Emili, W. C. Chan, *ACS Nano* **2014**, *8*, 2439.
- [10] A. Salvati, A. S. Pitek, M. P. Monopoli, K. Prapainop, F. B. Bombelli, D. R. Hristov, P. M. Kelly, C. Aberg, E. Mahon, K. A. Dawson, *Nat. Nanotechnol.* **2013**, *8*, 137.
- [11] S. Milani, F. B. Bombelli, A. S. Pitek, K. A. Dawson, J. Radler, *ACS Nano* **2012**, *6*, 2532.
- [12] H. Wang, R. Ma, K. Nienhaus, G. U. Nienhaus, *Small* **2019**, *15*, 1900974.
- [13] a) S. Dominguez-Medina, J. Blankenburg, J. Olson, C. F. Landes, S. Link, *ACS Sustainable Chem. Eng.* **2013**, *1*, 833; b) S. Balog, L. Rodriguez-Lorenzo, C. A. Monnier, M. Obiols-Rabasa, B. Rothen-Rutishauser, P. Schurtenberger, A. Petri-Fink, *Nanoscale* **2015**, *7*, 5991.
- [14] a) A. M. Davidson, M. Brust, D. L. Cooper, M. Volk, *Anal. Chem.* **2017**, *89*, 6807; b) R. M. Wang, L. Chen, D. X. Li, R. X. Liu, G. L. Ge, *Part. Part. Syst. Character.* **2017**, *34*, 1700134; c) M. Waghmare, B. Khade, P. Chaudhari, P. Dongre, *J. Nanopart. Res.* **2018**, *20*, 185.
- [15] P.-L. Latreille, M. Le Goas, S. Salimi, J. Robert, G. De Crescenzo, D. C. Boffito, V. A. Martinez, P. Hildgen, X. Banquy, *ACS Nano* **2022**, *16*, 1689.
- [16] D. Docter, U. Distler, W. Storck, J. Kuharev, D. Wunsch, A. Hahlbrock, S. K. Knauer, S. Tenzer, R. H. Stauber, *Nat. Protoc.* **2014**, *9*, 2030.
- [17] J.-M. Rabanel, J. Faivre, S. F. Tehrani, A. Lalloz, P. Hildgen, X. Banquy, *ACS Appl. Mater. Interfaces* **2015**, *7*, 10374.
- [18] C. Weber, S. Morsbach, K. Landfester, *Angew. Chem., Int. Ed. Engl.* **2019**, *58*, 12787.
- [19] a) E. Casals, T. Pfaller, A. Duschl, G. J. Oostingh, V. Puentes, *ACS Nano* **2010**, *4*, 3623; b) E. Casals, T. Pfaller, A. Duschl, G. J. Oostingh, V. F. Puentes, *Small* **2011**, *7*, 3479.
- [20] J. Piella, N. G. Bastus, V. Puentes, *Bioconjugate Chem.* **2017**, *28*, 88.
- [21] M. H. Cui, R. X. Liu, Z. Y. Deng, G. L. Ge, Y. Liu, L. M. Xie, *Nano Res.* **2014**, *7*, 345.
- [22] C. Röcker, M. Pötzl, F. Zhang, W. J. Parak, G. U. Nienhaus, *Nat. Nanotechnol.* **2009**, *4*, 577.
- [23] H. Wang, L. Shang, P. Maffre, S. Hohmann, F. Kirschhofer, G. Brenner-Weiss, G. U. Nienhaus, *Small* **2016**, *12*, 5836.
- [24] L. Shang, G. U. Nienhaus, *Acc. Chem. Res.* **2017**, *50*, 387.
- [25] a) A. Bekdemir, F. Stellacci, *Nat. Commun.* **2016**, *7*, 13121; b) A. Bekdemir, S. Y. Liao, F. Stellacci, *Colloids Surf., B* **2019**, *174*, 367.
- [26] R. Cerbino, V. Trappe, *Phys. Rev. Lett.* **2008**, *100*, 188102.
- [27] P. J. Lu, F. Giavazzi, T. E. Angelini, E. Zaccarelli, F. Jargstorff, A. B. Schofield, J. N. Wilking, M. B. Romanowsky, D. A. Weitz, R. Cerbino, *Phys. Rev. Lett.* **2012**, *108*, 218103.
- [28] a) L. G. Wilson, V. A. Martinez, J. Schwarz-Linek, J. Tailleur, G. Bryant, P. N. Pusey, W. C. K. Poon, *Phys. Rev. Lett.* **2011**, *106*, 018101; b) D. Germain, M. Leocmach, T. Gibaud, *Am. J. Phys.* **2016**, *84*, 202; c) V. A. Martinez, R. Besseling, O. A. Croze, J. Tailleur, M. Reufer, J. Schwarz-Linek, L. G. Wilson, M. A. Bees, W. C. K. Poon, *Biophys. J.* **2012**, *103*, 1637.
- [29] K. He, M. Spannuth, J. C. Conrad, R. Krishnamoorti, *Soft Matter* **2012**, *8*, 11933.
- [30] D. M. Wulstein, K. E. Regan, R. M. Robertson-Anderson, R. McGorty, *Opt. Express* **2016**, *24*, 20881.
- [31] M. Reufer, V. A. Martinez, P. Schurtenberger, W. C. K. Poon, *Langmuir* **2012**, *28*, 4618.
- [32] a) P.-L. Latreille, V. Adibnia, A. Nour, J.-M. Rabanel, A. Lalloz, J. Arlt, W. C. K. Poon, P. Hildgen, V. A. Martinez, X. Banquy, *Nat. Commun.* **2019**, *10*, 4294; b) V. Adibnia, M. Mirbagheri, P.-L. Latreille, J. Faivre, B. Cécycy, J. Robert, J.-F. Bouchard, V. A. Martinez, T. Delair, L. David, D. K. Hwang, X. Banquy, *Acta Biomater.* **2019**, *99*, 211.
- [33] F. Ferri, A. D'Angelo, M. Lee, A. Lotti, M. C. Pigazzini, K. Singh, R. Cerbino, *Eur. Phys. J.: Spec. Top.* **2011**, *199*, 139.
- [34] A. V. Bayles, T. M. Squires, M. E. Helgeson, *Soft Matter* **2016**, *12*, 2440.
- [35] W. S. Price, F. Tsuchiya, Y. Arata, *J. Am. Chem. Soc.* **1999**, *121*, 11503.
- [36] F. Giavazzi, D. Brogioli, V. Trappe, T. Bellini, R. Cerbino, *Phys. Rev. E* **2009**, *80*, 031403.
- [37] M. D. Haw, W. C. K. Poon, P. N. Pusey, *Phys. Rev. E* **1997**, *56*, 1918.
- [38] M. Y. Lin, H. M. Lindsay, D. A. Weitz, R. C. Ball, R. Klein, P. Meakin, *Nature* **1989**, *339*, 360.
- [39] S. T. Moerz, A. Kraegeloh, M. Chanana, T. Kraus, *ACS Nano* **2015**, *9*, 6696.
- [40] M.-M. Yin, W.-Q. Chen, Y.-Q. Lu, J.-Y. Han, Y. Liu, F.-L. Jiang, *Nanoscale* **2020**, *12*, 4573.
- [41] a) P. d. Pino, B. Pelaz, Q. Zhang, P. Maffre, G. U. Nienhaus, W. J. Parak, *Mater. Horiz.* **2014**, *1*, 301; b) J. Huhn, C. Fedeli, Q. Zhang, A. Masood, P. Del Pino, N. M. Khashab, E. Papini, W. J. Parak, *Int. J. Biochem. Cell Biol.* **2016**, *75*, 148.
- [42] a) I. Yadav, V. K. Aswal, J. Kohlbrecher, *Phys. Rev. E* **2016**, *93*, 052601; b) W. R. Krigbaum, F. R. Kuegler, *Biochemistry* **1970**, *9*, 1216.
- [43] D. P. Sun, D. I. Liao, S. J. Remington, **1989**, *86*, 5361.
- [44] a) S. M. Slack, T. A. Horbett, *J. Biomater. Sci., Polym. Ed.* **1991**, *2*, 227; b) S. M. Slack, T. A. Horbett, *ACS Symp. Ser.* **1995**, *602*, 112.
- [45] a) H. Mohammad-Beigi, Y. Hayashi, C. M. Zeuthen, H. Eskandari, C. Scavenius, K. Juul-Madsen, T. Vorup-Jensen, J. J. Enghild, D. S. Sutherland, *Nat. Commun.* **2020**, *11*, 4535; b) M. Lundqvist, J. Stigler, G. Elia, I. Lynch, T. Cedervall, K. A. Dawson, *Proc. Natl. Acad. Sci. USA* **2008**, *105*, 14265.
- [46] a) X. M. He, D. C. Carter, *Nature* **1992**, *358*, 209; b) A. Bujacz, *Acta Crystallogr., Sect. D: Biol. Crystallogr.* **2012**, *68*, 1278.
- [47] M. Mahmoudi, A. M. Abdelmonem, S. Behzadi, J. H. Clement, S. Dutz, M. R. Ejtehadi, R. Hartmann, K. Kantner, U. Linne, P. Maffre, S. Metzler, M. K. Moghadam, C. Pfeiffer, M. Rezaei, P. Ruiz-Lozano, V. Serpooshan, M. A. Shokrgozar, G. U. Nienhaus, W. J. Parak, *ACS Nano* **2013**, *7*, 6555.
- [48] P. Maffre, S. Brandholt, K. Nienhaus, L. Shang, W. J. Parak, G. U. Nienhaus, *Beilstein J. Nanotechnol.* **2014**, *5*, 2036.
- [49] a) K. Partikel, R. Korte, D. Mulac, H.-U. Humpf, K. Langer, *Beilstein J. Nanotechnol.* **2019**, *10*, 1002; b) C. Gräfe, A. Weidner, M. v.d. Lühe, C. Bergemann, F. H. Schacher, J. H. Clement, S. Dutz, *Int. J. Biochem. Cell Biol.* **2016**, *75*, 196.
- [50] O. Vilanova, J. J. Mittag, P. M. Kelly, S. Milani, K. A. Dawson, J. O. Radler, G. Franzese, *ACS Nano* **2016**, *10*, 10842.
- [51] S. Winzen, K. Koynov, K. Landfester, K. Mohr, *Colloids Surf., B* **2016**, *147*, 124.
- [52] C. Pisani, J. C. Gaillard, M. Odorico, J. L. Nyalosaso, C. Charnay, Y. Guari, J. Chopineau, J. M. Devoisselle, J. Armengaud, O. Prat, *Nanoscale* **2017**, *9*, 1840.
- [53] K. M. Tsoi, S. A. MacParland, X.-Z. Ma, V. N. Spetzler, J. Echeverri, B. Ouyang, S. M. Fadel, E. A. Sykes, N. Golaracena, J. M. Kathis, J. B. Conneely, B. A. Alman, M. Selzner, M. A. Ostrowski,

- O. A. Adeyi, A. Zilman, I. D. McGilvray, W. C. W. Chan, *Nat. Mater.* **2016**, *15*, 1212.
- [54] K. K. Sørensen, J. Simon-Santamaria, R. S. McCuskey, B. Smedsrød, *Compr. Physiol.* **2015**, *5*, 1751.
- [55] F. Campbell, F. L. Bos, S. Sieber, G. Arias-Alpizar, B. E. Koch, J. Huwyler, A. Kros, J. Bussmann, *ACS Nano* **2018**, *12*, 2138.
- [56] K. Kwapiszewska, K. Szczepański, T. Kalwarczyk, B. Michalska, P. Patalas-Krawczyk, J. Szymański, T. Andryszewski, M. Iwan, J. Duszyński, R. Hołyst, *J. Phys. Chem. Lett.* **2020**, *11*, 6914.
- [57] G. Espinosa, I. López-Montero, F. Monroy, D. Langevin, **2011**, *108*, 6008.
- [58] a) S. Bicknese, N. Periasamy, S. B. Shohet, A. S. Verkman, *Biophys. J.* **1993**, *65*, 1272; b) J. T. Mika, A. J. Thompson, M. R. Dent, N. J. Brooks, J. Michiels, M. K. Kuimova, *Biophys. J.* **2016**, *111*, 1528; c) M. Kubánková, P. A. Summers, I. López-Duarte, D. Kiryushko, M. K. Kuimova, *ACS Appl. Mater. Interfaces* **2019**, *11*, 36307.
- [59] E. Moeendarbary, L. Valon, M. Fritzsche, A. R. Harris, D. A. Moulding, A. J. Thrasher, E. Stride, L. Mahadevan, G. T. Charras, *Nat. Mater.* **2013**, *12*, 253.
- [60] J. Sankaran, M. Manna, L. Guo, R. Kraut, T. Wohland, *Biophys. J.* **2009**, *97*, 2630.
- [61] M. Lundqvist, J. Stigler, T. Cedervall, T. Berggård, M. B. Flanagan, I. Lynch, G. Elia, K. Dawson, *ACS Nano* **2011**, *5*, 7503.
- [62] B. Ouyang, W. Poon, Y.-N. Zhang, Z. P. Lin, B. R. Kingston, A. J. Tavares, Y. Zhang, J. Chen, M. S. Valic, A. M. Syed, P. MacMillan, J. Couture-Senécal, G. Zheng, W. C. W. Chan, *Nat. Mater.* **2020**, *19*, 1362.
- [63] P. Maffre, K. Nienhaus, F. Amin, W. J. Parak, G. U. Nienhaus, *Beilstein J. Nanotechnol.* **2011**, *2*, 374.
- [64] F. Bertoli, D. Garry, M. P. Monopoli, A. Salvati, K. A. Dawson, *ACS Nano* **2016**, *10*, 10471.
- [65] J.-M. Rabanel, P.-A. Piec, S. Landri, S. A. Patten, C. Ramassamy, *J. Controlled Release* **2020**, *328*, 679.